

REPORT DOCUMENTATION PAGE				Form Approved OMB No. 0704-0188	
Public reporting burden for this collection of information is estimated to average 1 hour per response, including the time for reviewing instructions, searching existing data sources, gathering and maintaining the data needed, and completing and reviewing this collection of information. Send comments regarding this burden estimate or any other aspect of this collection of information, including suggestions for reducing this burden to Department of Defense, Washington Headquarters Services, Directorate for Information Operations and Reports (0704-0188), 1215 Jefferson Davis Highway, Suite 1204, Arlington, VA 22202-4302. Respondents should be aware that notwithstanding any other provision of law, no person shall be subject to any penalty for failing to comply with a collection of information if it does not display a currently valid OMB control number. PLEASE DO NOT RETURN YOUR FORM TO THE ABOVE ADDRESS.					
1. REPORT DATE (DD-MM-YYYY) February 2012		2. REPORT TYPE Journal Article		3. DATES COVERED (From - To)	
4. TITLE AND SUBTITLE Kr II Laser-Induced Fluorescence for Measuring Plasma Acceleration (Preprint)				5a. CONTRACT NUMBER	
				5b. GRANT NUMBER	
				5c. PROGRAM ELEMENT NUMBER	
6. AUTHOR(S) W.A. Hargus, Jr.; G.M. Azarnia; and M.R. Nakles				5d. PROJECT NUMBER	
				5f. WORK UNIT NUMBER Q0AZ	
7. PERFORMING ORGANIZATION NAME(S) AND ADDRESS(ES) Air Force Research Laboratory (AFMC) AFRL/RZSS 1 Ara Drive Edwards AFB CA 93524-7013				8. PERFORMING ORGANIZATION REPORT NUMBER	
9. SPONSORING / MONITORING AGENCY NAME(S) AND ADDRESS(ES) Air Force Research Laboratory (AFMC) AFRL/RZS 5 Pollux Drive Edwards AFB CA 93524-7048				10. SPONSOR/MONITOR'S ACRONYM(S)	
				11. SPONSOR/MONITOR'S NUMBER(S) AFRL-RZ-ED-JA-2012-069	
12. DISTRIBUTION / AVAILABILITY STATEMENT Approved for public release; distribution unlimited (PA #12179).					
13. SUPPLEMENTARY NOTES For publication in Review of Scientific Instruments.					
14. ABSTRACT We present the application of laser-induced fluorescence of singly ionized krypton as a diagnostic technique for quantifying the electrostatic acceleration within the discharge of a laboratory cross-field plasma accelerator also known as a Hall effect thruster, which has heritage as spacecraft propulsion. The 728.98 nm Kr II transition from the metastable $5d^4D_{7/2}$ to the $5p^4P^{\circ}_{5/2}$ was used for the measurement of laser-induced fluorescence within the plasma discharge. From these measurements, it is possible to measure velocity as the krypton ions are accelerated from near rest to approximately 21 km/s (190 eV). Ion temperature and the ion velocity distributions may also be extracted from the fluorescence data since available hyperfine splitting data allows for the Kr II $5d^4D_{7/2} - 5p^4P^{\circ}_{5/2}$ transition line shape to be modeled. From the analysis, the fluorescence lineshape appears to be a reasonable estimate for the relatively broad ion velocity distributions. However due to an apparent overlap of the ion creation and acceleration regions within the discharge, the distributed velocity distributions increase ion temperature determination uncertainty significantly. Using the most probable ion velocity as a representative, or characteristic, measure of the ion acceleration, overall propellant energy deposition and effective electric fields may be calculated. With this diagnostic technique, it is possible to nonintrusively characterize the ion acceleration both within the discharge and in the plume.					
15. SUBJECT TERMS					
16. SECURITY CLASSIFICATION OF:			17. LIMITATION OF ABSTRACT	18. NUMBER OF PAGES	19a. NAME OF RESPONSIBLE PERSON
a. REPORT	b. ABSTRACT	c. THIS PAGE			Dr. William R. Hargus, Jr.
Unclassified	Unclassified	Unclassified	SAR	13	19b. TELEPHONE NUMBER (include area code) N/A

Kr II Laser-Induced Fluorescence for Measuring Plasma Acceleration

W. A. Hargus, Jr.,^{1, a)} G. M. Azarnia,^{2, b)} and M. R. Nakles^{2, c)}

¹⁾AFRL/RZSS, Edwards AFB, CA, USA

²⁾ERC, Inc., Edwards AFB, CA, USA

(Dated: 15 March 2012)

We present the application of laser-induced fluorescence of singly ionized krypton as a diagnostic technique for quantifying the electrostatic acceleration within the discharge of a laboratory cross-field plasma accelerator also known as a Hall effect thruster, which has heritage as spacecraft propulsion. The 728.98 nm Kr II transition from the metastable $5d^4D_{7/2}$ to the $5p^4P_{5/2}^o$ was used for the measurement of laser-induced fluorescence within the plasma discharge. From these measurements, it is possible to measure velocity as the krypton ions are accelerated from near rest to approximately 21 km/s (190 eV). Ion temperature and the ion velocity distributions may also be extracted from the fluorescence data since available hyperfine splitting data allows for the Kr II $5d^4D_{7/2}$ - $5p^4P_{5/2}^o$ transition line shape to be modeled. From the analysis, the fluorescence lineshape appears to be a reasonable estimate for the relatively broad ion velocity distributions. However due to an apparent overlap of the ion creation and acceleration regions within the discharge, the distributed velocity distributions increase ion temperature determination uncertainty significantly. Using the most probable ion velocity as a representative, or characteristic, measure of the ion acceleration, overall propellant energy deposition and effective electric fields may be calculated. With this diagnostic technique, it is possible to nonintrusively characterize the ion acceleration both within the discharge and in the plume.

PACS numbers: Valid PACS appear here

Keywords: Hall effect thruster, Krypton Ion, Laser-induced fluorescence

I. INTRODUCTION

Due to the relative scarcity of xenon (~ 90 ppb in atmosphere¹) combined with increasing industrial use, a number of alternative propellants have been examined for use in electrostatic spacecraft propulsion thrusters. Of the various propellants examined, krypton appears one of the simplest to integrate into existing systems. Krypton has a lower atomic mass (83.8 amu), but a slightly higher ionization potential (14.0 eV) than xenon. Like xenon, krypton is a noble gas and may be easily integrated into existing spacecraft propellant management systems without significant modification. Similar ionization potentials should not dramatically affect Hall effect thruster efficiency, and the lower atomic mass could potentially produce a 25% increase in specific impulse due to the increased propellant exit velocity of lighter ions. Krypton is also approximately $10\times$ more common in the atmosphere (and hence in production) than xenon, and when accounting for mass is approximately $6\times$ less expensive. Table I summarizes the properties of xenon and krypton relevant for electrostatic spacecraft propulsion.¹

In order to assess krypton propellant electrostatic plasma accelerators such as Hall effect thrusters, minimally invasive diagnostic techniques capable of mea-

TABLE I. Comparison of xenon and krypton properties critical for electrostatic propulsion.¹

Property	Units	Xe	Kr
Atomic Mass	amu	131.3	83.8
1 st Ionization Energy	eV	12.1	14.0
2 nd Ionization Energy	eV	21	24
3 rd Ionization Energy	eV	32	37
Atmospheric Concentration	ppb	87	1000
Stable Isotopes		9	6
Odd Isotopes		2	1
Critical Pressure	MPa	5.84	5.50
Critical Temperature	K	290	209
Boiling Point (1 atm)	K	161	120

suring the electrostatic acceleration of the Kr II must be developed. Similar measurements have been used for xenon fueled electrostatic thrusters for a number of years^{2,3}. This work examines theoretical development and application of laser-induced fluorescence (LIF) of a singly charged krypton ion (Kr II) transition within a laboratory Hall effect plasma accelerator.

II. LASER-INDUCED FLUORESCENCE

Laser-induced fluorescence (LIF) may be used to measure velocity-induced shifts in the spectral absorption of various plasma species with high spatial resolution⁴. The fluorescence is collected as a laser is tuned in frequency over the transition of interest, of energy $h\nu_{12}$,

^{a)}Electronic mail: william.hargus@edwards.af.mil.

^{b)}Electronic mail: gregory.azarnia.ctr@edwards.af.mil.

^{c)}Electronic mail: michael.nakles.ctr@edwards.af.mil.

where h is Plank's constant, ν_{12} is wavenumber of transition between lower state 1 and higher energy state 2. Note that state 1 may be the ground state, but any sufficiently highly populated excited state will do. In this work, we have chosen to examine a metastable state to maximize signal levels at optically accessible transitions in our low density plasma plume ($< 10^{18} \text{ m}^{-3}$). These measurements also provide high spatial resolution, determined by the intersection of the probe laser beam with the fluorescence optical collection volume.

Velocity measurements may be made using LIF velocimetry as an atom, or as in our case an ion, population moving with a velocity component u relative to the direction of the incoming laser will absorb photons at a frequency shifted from that of stationary absorbers due to the Doppler effect. The magnitude of this frequency shift $\delta\nu_{12}$ is

$$\delta\nu_{12} = \frac{u}{c}\nu_{12}. \quad (1)$$

LIF is minimally invasive compared to electrostatic probes as it does not significantly disturb the discharge. The LIF fluorescence signal is a convolution of the velocity distribution function (VDF), transition lineshape, and laser beam frequency profile. Determination of the VDF from LIF data only requires the deconvolution of the transition lineshape and laser beam profile from the raw fluorescence.

The fluorescence lineshape may also provide valuable information on the state of the plasma, such as electron density, pressure, or heavy species temperature. In the somewhat turbulent plasmas typical of Hall effect thrusters, the fluorescence lineshape can also be indicative of the relative motion of the ionization zone as it axially traverses in the periodic breathing mode plasma fluctuation.^{5,6} However, care must be taken to ensure that the relative effects of these phenomena are separable. In addition, magnetic (Zeeman effect) and electric (Stark effect) fields may also influence the fluorescence lineshape⁷ and must be accounted for when analyzing the lineshapes should the fields be of sufficient magnitude. In the case of LIF of ions within a Hall effect thruster, the fluorescence lineshape appears to be most indicative of the aforementioned plasma turbulence including periodicity in the positions of the ionization zone within the acceleration channel.

III. KRYPTON ION SPECTROSCOPY

A. Hyperfine Effects

Of the 31 known isotopes of Kr, only six have naturally occurring atmospheric concentrations greater than 0.3%. Of these six isotopes between 78 amu and 86 amu, only one, ⁸³Kr has an odd number of neutrons¹. This is

important in the high resolution analysis of atomic spectra since each will have a slight difference in their electron transition energies due to their differences in nuclear mass.⁸

TABLE II. Naturally Occurring Krypton Isotope Properties.^{1,9}

Mass (amu)	Abundance	Nuclear Spin
78	0.35%	0
80	2.27%	0
82	11.56%	0
83	11.55%	$\frac{9}{2}$
84	56.90%	0
86	17.37%	0

The odd mass isotopes are further spin split due to nuclear magnetic dipole and electric quadrupole moments. Nuclei which have an odd number of protons and/or an odd number of neutrons possess an intrinsic nuclear spin $\mathbf{I}\hbar/2\pi$, where \mathbf{I} is integral or half-integral depending on if the atomic mass is even or odd, respectively⁸ and bold-face is used to denote vector quantities. For nuclei with non-zero nuclear spin (angular momentum, \mathbf{J}), the interaction of the nucleus with the bound electrons lead to the splitting of levels with \mathbf{J} into a number of components, each corresponding to a specific value of the total angular momentum $\mathbf{F} = \mathbf{I} + \mathbf{J}$.¹⁰ As a result of this interaction, \mathbf{F} is a conserved quantity while \mathbf{I} and \mathbf{J} individually are not. The interaction is weak, allowing the hyperfine splitting of each level to be taken independently of the other levels. The number of nuclear spin split hyperfine components is $2I + 1$ if $J \geq 1$ and $2J + 1$ if $J < 1$, with F taking on the values $F = J + I, J + I - 1, \dots, |J - I|$ while satisfying the selection rules imposed on F , i.e. $\Delta F = 0, \pm 1$, unless $F = 0$, in which case $\Delta F \neq 0$.

With these selection rules on the quantum numbers for a particular electronic transition, and with knowledge of the hyperfine structure constants which characterize the magnetic dipole and electric quadrupole moments of the nucleus,⁸ the hyperfine energy shifts from the position of the energy for the unshifted level with angular momentum J can be easily calculated.^{11,12} The relative intensities of transitions between these levels are derived assuming Russel-Saunders coupling,¹¹ allowing the complete construction of the fluorescence lineshape. Of course, the intensities of the isotope shifted transitions are proportional to each isotopes relative abundance.

Two constants are associated with the magnitude of hyperfine nuclear spin splitting.⁸ These are the A hyperfine structure constant which represents the nuclear magnetic dipole effect on the atom, and the B hyperfine structure constant which is associated with the nuclear electric quadrupole moment of the atom which will only be present if $I \geq 1$. The relative energy of the spin split states depends on the sign of A . In atoms with $A > 0$, the state with the highest value of F has the highest energy. While for atoms with $A < 0$, the state with the

lowest value of F has the highest energy.¹¹ The energy level shift ΔE_M associated with the magnetic dipole of the nucleus is given by Cowan.⁸

$$\Delta E_M(F) = \frac{1}{2}A[F(F+1)J(J+1)I(I+1)] = \frac{A}{2}C \quad (2)$$

Additionally, the energy spacing between successive levels $F-1$ and F may be shown to be proportional to F .

$$\Delta E_M(F) - \Delta E_M(F-1) = AF \quad (3)$$

If $I \geq 1$, the nucleus will have an electric quadrupole moment and a related hyperfine splitting constant B which produces an additional hyperfine splitting with energy linear in $C(C+1)$ where C is previously defined in Eqn. 2.

$$\Delta E_F = \Delta E_M + \Delta E_Q \quad (4)$$

$$\Delta E_F = \frac{AC}{2} + \frac{B[\frac{3}{2}C(C+1)2I(I+1)J(J+1)]}{4I(2I-1)J(2J-1)} \quad (5)$$

Where ΔE_F is the combined nuclear spin split energy level shift combining the effect from the nuclear magnetic dipole moment ΔE_M and the effect of the electric quadrupole moment ΔE_Q .⁸ It should be noted that the center of gravity of the hyperfine levels lies at a position of the unsplit level J .¹⁰

$$\sum_F (2F+1)\Delta E_F \quad (6)$$

Due to close energy spacing of nuclear spin split levels, near ideal coupling between **I** and **J** occurs in most hyperfine structure. Therefore, the intensity S rules derived by White for Russel-Saunders coupling are appropriate for hyperfine splitting.¹¹

For $J-1 \rightarrow J$,

$F-1 \rightarrow F$:

$$S = \kappa \frac{(Q+I+1)(Q+I)(Q-I)(Q-I-1)}{F} \quad (7)$$

$F \rightarrow F$:

$$S = -\kappa \frac{(Q+I+1)(Q-I)(W+I)(W-I-1)(2F+1)}{F(F+1)} \quad (8)$$

$F+1 \rightarrow F$:

$$S = \kappa \frac{(W+I)(W+I-1)(W-I-1)(W-I-2)}{F+1} \quad (9)$$

For $J \rightarrow J$,

$F-1 \rightarrow F$:

$$S = -\kappa \frac{(Q+I+1)(Q-I)(W+I+1)(W-I)}{F} \quad (10)$$

$F \rightarrow F$:

$$S = \kappa \frac{[J(J+1) + F(F+1) + I(I+1)]^2(2F+1)}{F(F+1)} \quad (11)$$

$F+1 \rightarrow F$:

$$S = -\kappa \frac{(Q+I+2)(Q-I+1)(W+I)(W-I-1)}{(F+1)} \quad (12)$$

Where S is the transition strength and κ is an arbitrary constant. The variables $Q = J + F$ and $W = J - F$ are introduced to compress notation.

The relative intensities of the isotope shifted transitions are proportional to each isotope's relative abundance. However, the relative intensities of the nuclear spin split hyperfine splitting are governed by two summation rules¹⁰. First, the sum of the intensities of all the lines of the hyperfine structure of a transition $J \rightarrow J'$ originating from a component F of the level J is proportional to the statistical weight of this component, $(2F+1)$. Second, the sum of the intensities of all the lines of the hyperfine structure the transition $J \rightarrow J'$ ending on the component F' of the level J' is proportional to the statistical weight of this component, $(2F'+1)$. With these two sum rules, a system of linear equations are solved for the relative intensities of the nuclear spin split components of each isotope.

B. Kr II $5d^4D_{7/2}-5p^4P_{5/2}^\circ$ Transition at 728.98 nm

A survey of Kr II transitions has identified only the $5d^4D_{7/2}-5p^4P_{5/2}^\circ$ transition at 728.98 nm where both the isotope and spin split hyperfine constants have been measured.¹³ Scholl, et al.¹⁴ measured the lower $5d^4D_{7/2}$ state A and B spin splitting constants for ⁸³Kr to high accuracy as shown in Table III. While Schuessler et al.¹⁵ measured the spin splitting constants for the upper $5p^4P_{5/2}^\circ$ state also shown in Table III. Schuessler et al. also measured the isotope shifts of the 728.98 nm $5d^4D_{7/2}-5p^4P_{5/2}^\circ$ transition as shown in Table IV. From

TABLE III. Spin Splitting Constants for the $5d^4D_{7/2}-5p^4P_{5/2}^\circ$ ^{83}Kr II transition at 728.98 nm^{14,15}

Electronic State	A Coefficient MHz	B Coefficient MHz
$5d^4D_{7/2}$	-43.513	-294.921
$5p^4P_{5/2}^\circ$	-167.2	+91

TABLE IV. Isotope Shifts for the $5d^4D_{7/2}-5p^4P_{5/2}^\circ$ Kr II transition at 728.98 nm¹⁵

Isotope	Isotope Shift MHz
78	1185.7
80	768.0
82	372.6
83	175.0
84	0
86	-365.2

the $5p^4P_{5/2}^\circ$ state, there are 6 known fluorescence paths. From available Einstein coefficients for spontaneous emission, the transition $5s^4P_{5/2}-5p^4P_{5/2}^\circ$, at 473.90 nm has a $\sim 80\%$ branching ratio¹⁶. The resonant fluorescence for the $5d^4D_{7/2}-5p^4P_{5/2}^\circ$ transition appears to be $\sim 10\%$.

Using Tables III and IV, the line structure of the 728.98 nm $5d^4D_{7/2}-5p^4P_{5/2}^\circ$ transition may be modeled. We assume Doppler broadening to be the only significant broadening mechanism based on the low plasma number density.

Figure 1 shows the lineshape for a variety of temperatures, up to 10,000 K (0.85 eV). The hyperfine splitting is significant, and as a result, Fig. 1 shows an approximate 200 MHz broadening of the line cumulative full width at half maximum (FWHM) relative to the single component Doppler width. However, temperatures above 500 K do not exhibit any visible structure.

IV. APPARATUS

A. Vacuum Facility and Thruster

The measurements were performed in a cryogenically pumped, non-magnetic stainless steel vacuum chamber with a 1.8 m diameter and 3 m length. The measured pumping speed was 18,000 L/s on krypton. Background pressure during thruster operation was measured with a cold cathode ionization gauge to be 1×10^{-3} Pa, corrected for krypton (N_2 conversion to Kr pressure multiplicative factor of 0.59¹⁷).

The Hall effect thruster examined is a low power laboratory Hall effect thruster which has been described elsewhere^{3,18}. This thruster is designed for operation

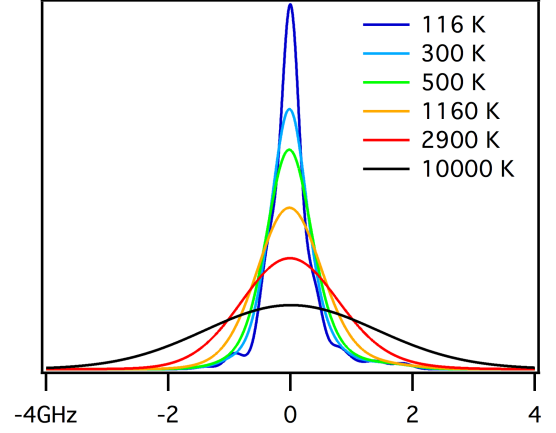


FIG. 1. Multitemperature spectrum of the Kr II 728.98 nm $5d^4D_{7/2}-5p^4P_{5/2}^\circ$ transition.

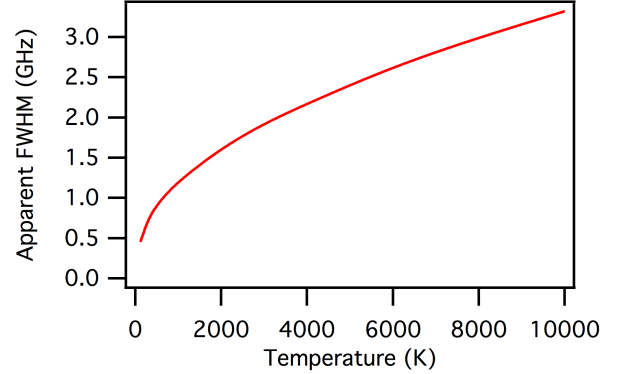


FIG. 2. Cumulative FWHM for the Kr II 728.98 nm $5d^4D_{7/2}-5p^4P_{5/2}^\circ$ transition.

on xenon and its performance is not characterized for krypton. Thruster operation for this effort consisted of a single stable condition. Compared to nominal operation on xenon, krypton operation was unstable at higher magnetic field strengths and lower flow rates. In order to match anode discharge potential to previous xenon measurements (250 V), the flow rate was increased by 24% and the current to the magnetic field was reduced to approximately half. The condition chosen for study also consisted of the lowest discharge current oscillation amplitude as determined by fixing the propellant flow rate and varying the magnetic field. At this krypton operating condition, the total anode current was only increased 15% implying a lower krypton propellant ionization efficiency than for xenon.

Within the vacuum chamber, the thruster is mounted on a three axis orthogonal computer controlled translation system, so that the sample volume position may be

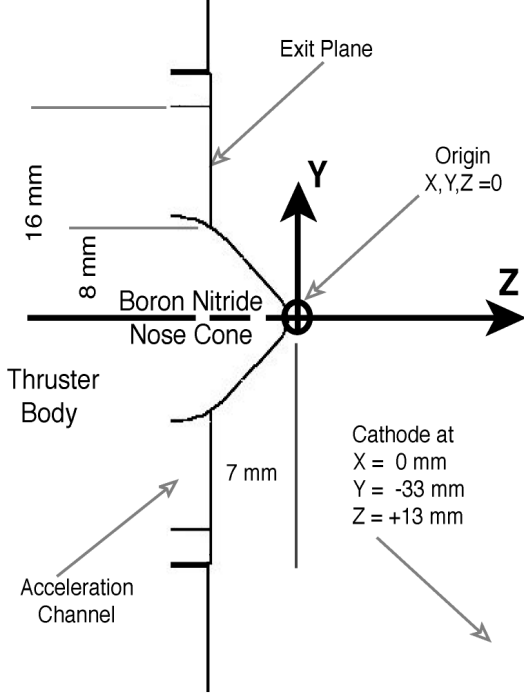


FIG. 3. Cross-section of the low power laboratory Hall effect thruster with origin of the coordinate system and positions of critical dimensions.

shifted relative to the fluorescence collection volume defined by the intersection of the probe beam waist and the collection optics focus. Figure 3 shows the geometry of the Hall effect thruster. The locations of the protruding central magnetic pole (nose cone) and geometry of the acceleration channel are indicated as is the position of the cathode exit. The cartesian coordinate system and origin used in these measurements is also shown. The coordinate system origin is 0.5 mm beyond the tip of the nose cone due to the repeatability with which this position may be located. All locations are referenced to these Cartesian coordinates with the indicated origin.

B. Laser and Optics

Upon selection of the Kr II $5d^4D_{7/2}-5p^4P_{5/2}^o$ transition at 728.98 nm ($\Delta E = 13,713.989 \text{ cm}^{-1}$), we purchased a custom ± 50 GHz Littman-Metcalf external cavity tunable diode laser centered on the $5d^4D_{7/2}-5p^4P_{5/2}^o$ transition with a maximum output power of 25 mW. This laser is capable of mode hop free tuning across approximately 100 GHz tuning range with a line width of less

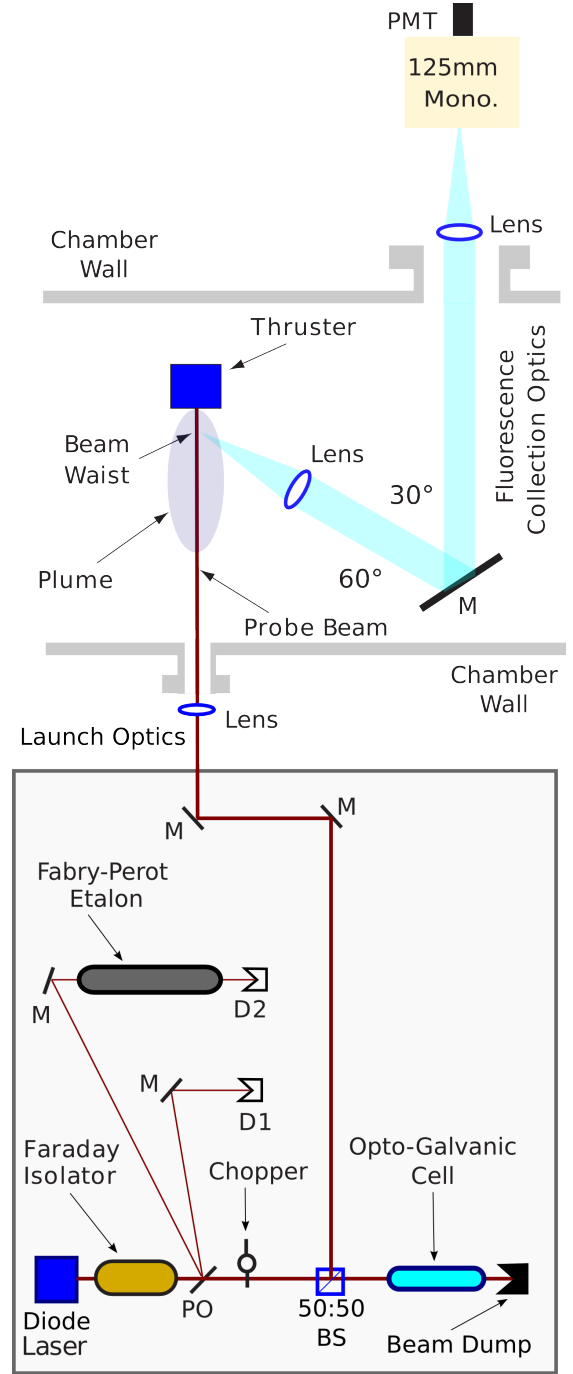


FIG. 4. Layout of Kr II laser-induced fluorescence apparatus showing all relevant optical components, portions of the vacuum chamber, and Hall effect thruster thruster plume.

than 500 kHz.

Based on previous efforts,³ the laser, probe beam launch optics, and fluorescence collection optics are located on two optical tables placed about viewports with optical access into the vacuum chamber as shown in Fig. 4. On the primary optics table, the diode laser beam first passes through a Faraday isolator to eliminate laser

cavity feedback. The laser beam then passes through a wedged beam pick-off (PO) to provide beam diagnostics. The first of the two reflections (each approximately 5% of incident power) is directed onto a photodiode detector (D1) and provides constant power feedback to the laser. The second pick-off beam passes through a 300 MHz free spectral range, high finesse (~ 200) Fabry-Perot etalon (F-P) that provides frequency monitoring of the wavelength interval swept during a laser scan.

The main laser beam is then chopped at 3 kHz by a mechanical optical chopper to allow for phase sensitive signal detection. It is then divided into two equal components by a 50:50 cube beam splitter (BS). The first component passes through a krypton opto-galvanic cell and is terminated by a beam dump. The opto-galvanic cell current is capacitively coupled to a lock-in amplifier in order to monitor the Kr II 728.98 nm $5d^4D_{7/2}-5p^4P_{5/2}^o$ transition thereby providing a zero velocity reference.¹⁹

The probe beam is then directed via several mirrors and focused by a single lens to a sub-millimeter beam waist within the chamber vacuum through a glass vacuum viewport. The fluorescence collection optics also shown in Fig. 4 collect and filter the signal generated at the beam waist. The fluorescence is collected by a 75 mm diameter, 300 mm focal length lens within the chamber. The collimated signal is directed through a window in the chamber side wall to a similar lens that focuses the collected fluorescence onto the entrance slit of 125 mm focal length monochromator with a photomultiplier tube (PMT) detector. The PMT signal is then analyzed using a second lock-in amplifier. The spatial resolution of the measurements is determined by the geometry of the spectrometer entrance slit (note the 1:1 magnification of the collection optics) and for our measurements consists of a cylinder 0.2-0.5 mm in diameter by 0.5 mm in length.

V. MEASUREMENTS AND ANALYSIS

Measurements in this work are limited to the $Z - Y$ plane shown in Fig. 3. Two regions of LIF measurements are presented. The first measurement region is along $Y = +12$ mm, which corresponds to the center of the upper portion of the annular acceleration channel. These axial velocity measurements are between $Z = 0$, the extent of the protruding central pole nose cone; and $Z = -13$ mm, the furthest into the thruster that is optically accessible with the collection optics shown in Fig. 4. This set of measurements characterizes the acceleration within the thruster and into the near-plume region.

The second measurement set is a radial survey of the axial ion velocities at the cathode plane ($Z = +13$ mm) varying radially from near the cathode ($Y = -30$ mm) to a congruent distance in the positive axis (upward to $Y = +40$ mm). This plume measurement set, 20 mm from the exit plane, provides insight into the near-field plume evolution and shows the interaction of annular plasma source.

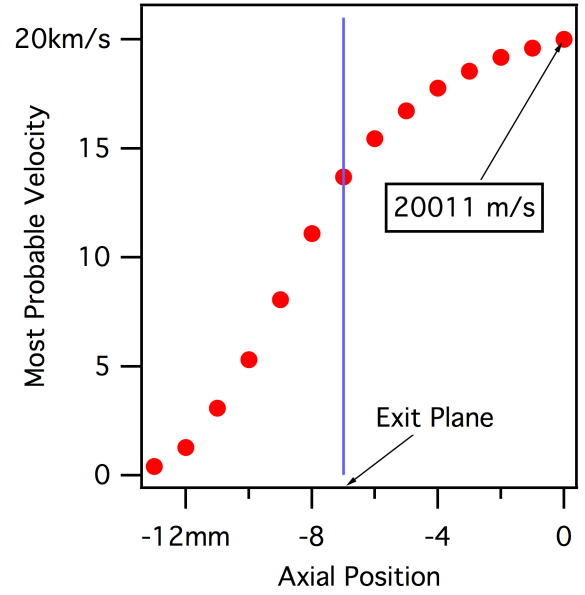


FIG. 5. Most probable velocities as determined from the peak of each fluorescence trace along acceleration channel center-line ($Y = +12$ mm).

A. Acceleration within Thruster and Near-Plume

This measurement region is limited to a line at $Y = +12$ mm (corresponding to the center of the acceleration channel) between $Z = 0$ (the furthest axial extent of the boron nitride nose cone) and $Z = -13$ mm (corresponding to furthest interior optical access provided by the apparatus). This region of the plasma discharge is of interest since it corresponds to region of ionization and acceleration for a majority of the ions produced by the cross-field acceleration within a Hall effect thruster.

Figure 5 shows the *most probable velocity* (defined as the peak of the velocity distribution) measured at the acceleration channel center ($Y = +12$ mm) between the tip of the nose cone ($Z = 0$) and the deepest optical access ($Z = -13$ mm), 6 mm within the thruster. In these data, we see a smooth increase in velocity from near 0 m/s, deep within the thruster, to approximately 20 km/s at $Z = 0$, which denotes the furthest axial extent of the nose cone. From these data, we see that approximately 70% of the acceleration occurs within the physical confines of the thruster. However, significant acceleration also occurs in the near-plume just outside the annular thruster acceleration channel.

Similarly, Fig. 6 shows the variation of Kr II kinetic energy as calculated from the peaks of the fluorescence traces. We deem this to be the *most probable ion kinetic energy*. From these data, we see that the majority of the energy deposition into the ionized propellant is external. The ion energies are only approximately 80 eV at the exit plane and reach approximately 175 eV by the axial extent of the nose cone. Interestingly, the peak ion energy

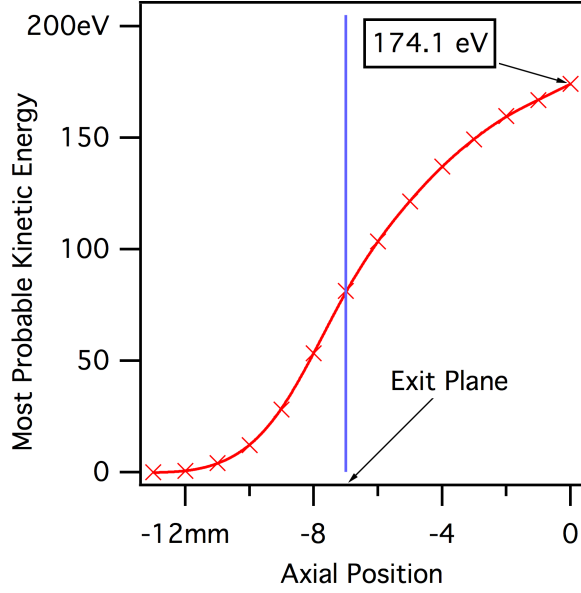


FIG. 6. Most probable kinetic energies as determined from most probable velocities along acceleration channel centerline ($Y = 12$ mm).

at $Y = \pm 12$ mm at $Z = 13$ mm is approximately 190 eV. Therefore, this limited data set captures the majority of the axial propellant energy deposition.

Calculating most probable ion kinetic energies from the most probable velocities, also allows us to determine the magnitudes of the effective electric field acting on the ions. As shown on Fig. 6, this calculation is performed by fitting a smoothing spline to these data and then differentiating. This produces an approximation of the effective electric field accelerating the Kr II propellant as shown in Fig. 7. Here, the calculated effective electric field peaks at 28 kV/m approximately 1 mm within the annular acceleration channel. The electric field variation is steepest within the interior and decreases more gradually in the plume, paralleling the radial magnetic field strength, which strongly influences plasma conductivity.

Figure 8 shows the raw fluorescence traces mapped from frequency detuning to velocity space. These data correspond to the velocities in Fig. 5 and span the same spatial range. Please note that the relative ratios of the signals are not directly comparable since these data are scaled to unity area and not scaled between the traces. The value of this presentation is that the raw fluorescence traces approximate the ion velocity distributions. Unity area normalization allows us to illustrate the acceleration of these ions within each sample irrespective of partial occlusion of the collection optics.

Comparison of the various traces in Fig. 8 does provide a qualitative understanding of the ionization and acceleration process in this thruster. At the furthest into the thruster that affords optical access ($Z = -13$ mm), we see a very sharp peak with a small positive velocity. Here,

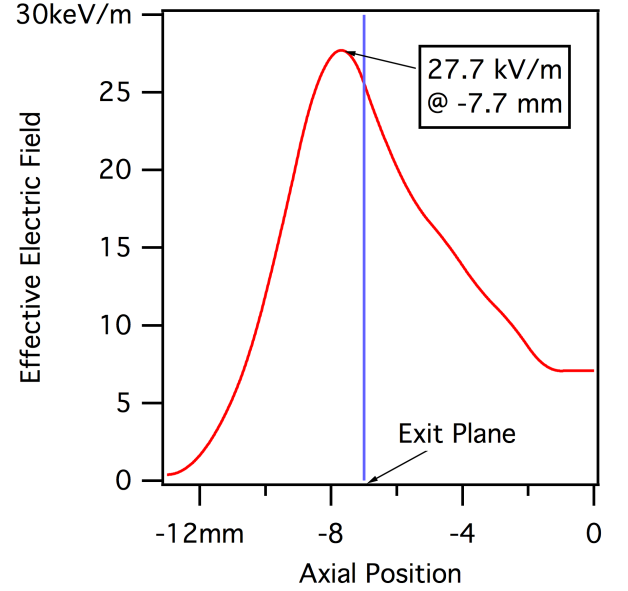


FIG. 7. Effective electric field as calculated from most probable kinetic energies along acceleration channel centerline ($Y = 12$ mm).

the ionization process is occurring and substantial acceleration of the ions has not yet occurred. The height of this peak drops substantially and the distribution broadens until approximately $Z = -9$ mm. In this region, we hypothesize that the acceleration and ionization regions overlap substantially. This is consistent with the traces in Fig. 8 between $Z = -13$ mm and $Z = -9$ mm where a continuum of stationary to accelerated ions is clearly shown.

Interestingly, $Z = -8$ mm is also the peak of the calculated effective electric field, and at this position, the character of the velocity distributions (as characterized by the fluorescence traces in Fig. 8) changes. At this position and further downstream, the main peak continues to accelerate as shown by the implied VDFs in Fig. 8 and the most probable velocities in Fig. 5. The peak also sharpens slightly possibly due to small amount of kinematic compression. However, the velocity distributions (as approximated by the raw fluorescence traces) now develop a low level plateau between zero velocity and the main peak. This plateau implies that there is still some ionization occurring. However, it appears that the primary ionization zone has passed, and that only residual ionization is occurring in this region. Obviously, these late stage ions will not recover substantial portions of the applied acceleration potential and will continually lag the primary ion velocity population, thereby broadening the VDF.

Beyond $Z = -5$ mm (2 mm outside the geometrical channel exit plane), the apparent velocity distributions in Fig. 8 retain a near constant peak magnitude with some acceleration (most visible in Fig. 5. The low level

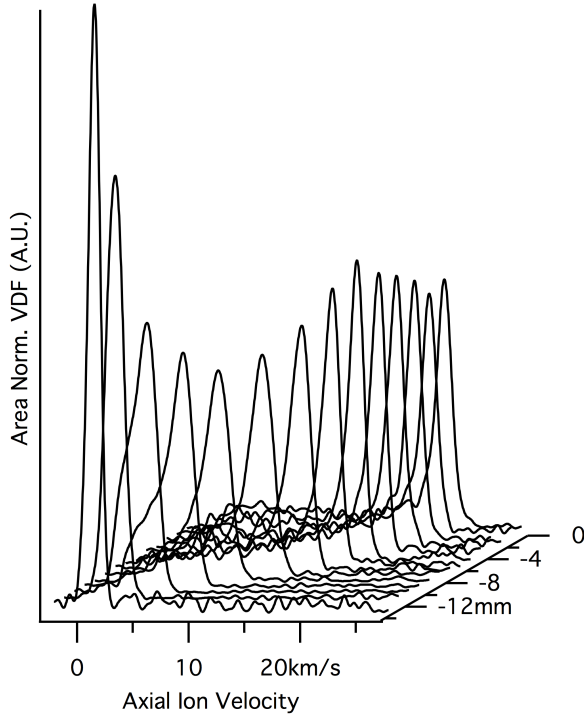


FIG. 8. Scaled fluorescence lineshape illuminating the ionization and acceleration process within the acceleration channel centerline ($Y = +12$ mm) along the Z axis. Note that these data traces are each scaled to unity area and that the exit plane is at $Z = -7$ mm.

plateau feature remains constant implying the presence of external ionization. The source of the neutrals may either be from background pressure of the vacuum facility or from neutrals passing through the thruster without being ionized.

Comparison to previous xenon ion LIF measurements of the same thruster,³ indicate that these krypton distributions are considerably narrower and exhibit improved SNR. This could be due to a number of factors. For one, this data set was taken with a minimized discharge oscillation for thruster operational stability. Previous LIF studies have shown that the magnitude of the breathing mode oscillation is correlated to the width of the velocity distributions. Therefore, reducing discharge channel plasma turbulence will likewise reduce the breadth of the VDF.⁵ Krypton operation also typically displays lower magnitude breathing mode discharge oscillations,²⁰ likely due to differences in the electron mobility, perhaps due to the lower mass, greater mobility of krypton. As a result of most likely a combination of these factors, the krypton LIF traces in this study are typically much sharper and exhibit higher SNR than many previous xenon LIF measurements. Future measurements at conditions optimized for thruster performance may yield results with optimized signals.

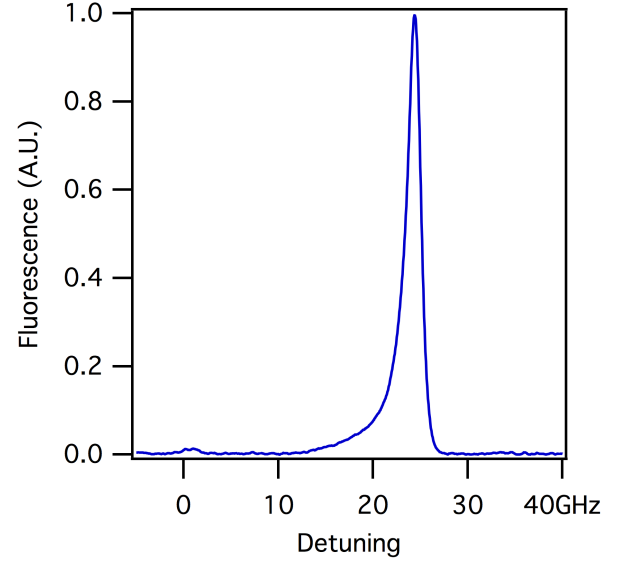


FIG. 9. Laser-induced fluorescence collected at $Y = 0$ mm, $Z = +13$ mm. Note the very small peak near 0 GHz and the main peak at 33 GHz detuning from stationary line center.

B. Plume at Cathode Plane

Figure 9 shows the collected fluorescence at $Y = 0$, $Z = -13$ mm. At this location, we see very good signal to noise ratios (SNR) and a distinct peak shifted approximately 33 GHz from the stationary reference. This shift corresponds to an axial velocity of 17,800 m/s. Also interesting is a small peak with a much smaller magnitude corresponding to a velocity of approximately 500 m/s. Multiple peaks are not unique to this position and have been seen in LIF measurements in prior efforts^{18,21}. It is also often difficult to ascribe a singular velocity, or even several velocities, to a measurement. Rather, it is necessary, even in a simple lineshape like that shown in Fig. 9, to consider a continuous distribution of velocities²².

Accepting that the (sometimes multiple) peaks from the fluorescence distributions represent appropriate assessments of the most probable velocities, we can find the most probable velocities from peaks in the fluorescence traces. Figure 10 shows the velocities calculated from the identifiable peaks in all the LIF traces in the cathode plane radial cross-section measurement set. As seen in Fig. 10, the plume structure evolves as one departs from the $Y = 0$, $Z = +13$ mm trace shown in Fig. 9.

Examining Fig. 10 shows three peak classes identified by our analysis. The peaks with the highest magnitude (velocity as well as signal strength) appears to be clearly due to the primary population from the nearest portion of the acceleration channel annulus. It is also always the largest in magnitude. The intermediate peak as illustrated by our previous geometrical argument appears to be a population from the further portion of the acceleration channel annulus. It generally is the second peak

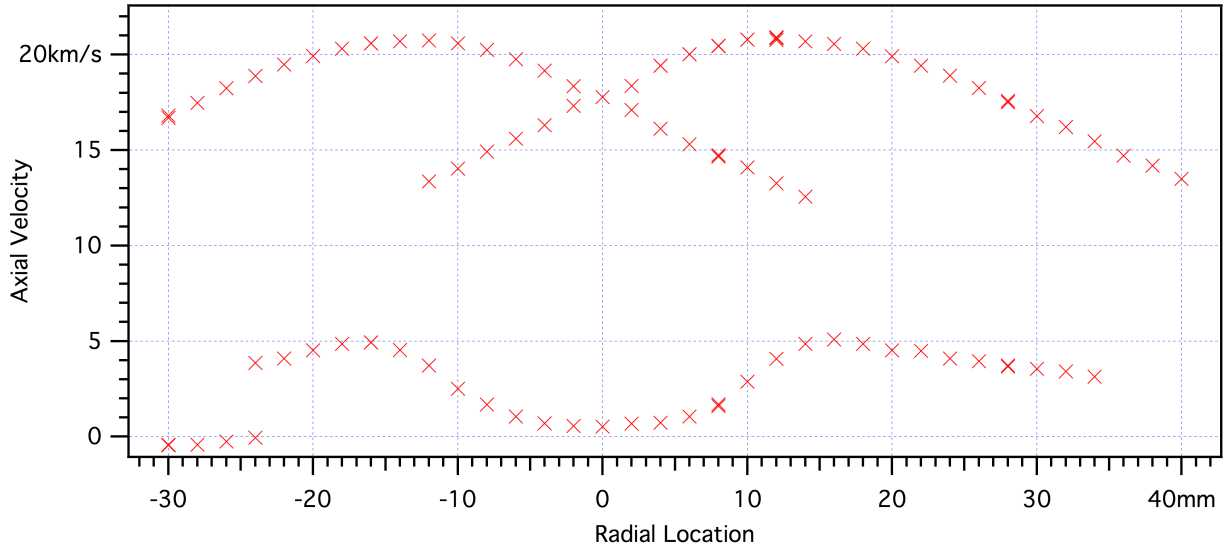


FIG. 10. Axial most probable velocities of all distinguishable peaks in each fluorescence trace at $Z = 13$ mm (20 mm into plume from the exit plane at the geometrical cathode plane).

in magnitude, especially nearest the thruster centerline. The third peak is less well understood and may be due to late ionization, plume collisions producing a population of ions with low Z axis velocity component, or some combination of these two mechanisms.

The influence of the annular structure of the Hall effect thruster is visible in the velocities identified in the plume in Fig. 10. This is most obvious in the distinct expansion of the two overlapping plumes. The ion populations overlap and due to the low densities in the plasma plume there is clear evidence of populations from each side of the annulus when one examines the various velocity peaks as illustrated in Fig. 10. Here, the peak velocities correlate to the value at $Y = \pm 12$ mm, the geometric center of the annular acceleration channel. For example, the $Y = +12$ mm axial velocity of 20.8 km/s can be compared to the axial velocity of the intermediate velocity peak at $Y = -12$ mm, 13.4 km/s. These values match the expected component due to the 40° angle between the measurement axis and the geometrical distance from the exit plane ($\Delta Y = 24$ mm and $\Delta Z = 20$ mm). This appears to link the first two classes of peaks as an annular expansion in a low collisional density regime.

As shown in Fig. 9, the relative magnitudes of the various peaks can vary significantly. Figure 11 shows how the lineshape with its multiple peaks evolves, starting on the plume centerline and moving outward. On centerline, the highest velocity peak dominates and the slow peak is only evident upon very close examination as in Fig. 9. The highest velocity peak dominates all the subsequent measurements away from the plume centerline with an peak velocity that reaches its maximum at the geometric center of each annular acceleration channel at $Y = \pm 12$ mm as shown in Fig. 10. This maximum signal peak always corresponds to the highest axial velocity,

and is clearly due to the ions from the nearest portion of the acceleration channel for each measurement.

The intermediate velocity peaks in Fig. 11 appears to overlap the high velocity peak on centerline as shown in Fig. 9. At measurements away from plume centerline, these intermediate peaks' magnitude and velocity drop. By $Y = \pm 16$ mm, this velocity population feature is no longer distinguishable in the fluorescence traces. This class of peaks is consistent the flux of ions emanating from the opposite side of the acceleration channel annulus from the measurement. This appears consistent with close examination of Fig. 10 in comparison with Fig. 11 from which much of this behavior becomes evident and is geometrically consistent.

The lowest velocity peaks seen in Fig. 11 increases in velocity, and relative magnitude as the measurements move away from the plume centerline. Interestingly, the velocity reaches a maximum near the annular acceleration channel geometric outer edge at $Y = \pm 16$ mm. This low velocity feature is believed to be at least partially due to a late ionization population consistent with internal velocity measurements. This is supported by the broad population of ions between the highest energy and the zero velocity that appears to some extent in all the traces. In addition, there is likely sufficient collisionality in the near-plume that may contribute to this feature this.

This low velocity population component varies from approximately 500 m/s on centerline to a peak of 5 km/s at $Y = \pm 15$ mm, decreasing slightly at larger radii. The low velocities of this population near the centerline are likely due to the protruding nose cone physically impeding ion flux as well as the annular geometry of the Hall effect thruster. The abrupt change in the velocities at $Y = -24$ mm is due to the cathode ejecting a popula-

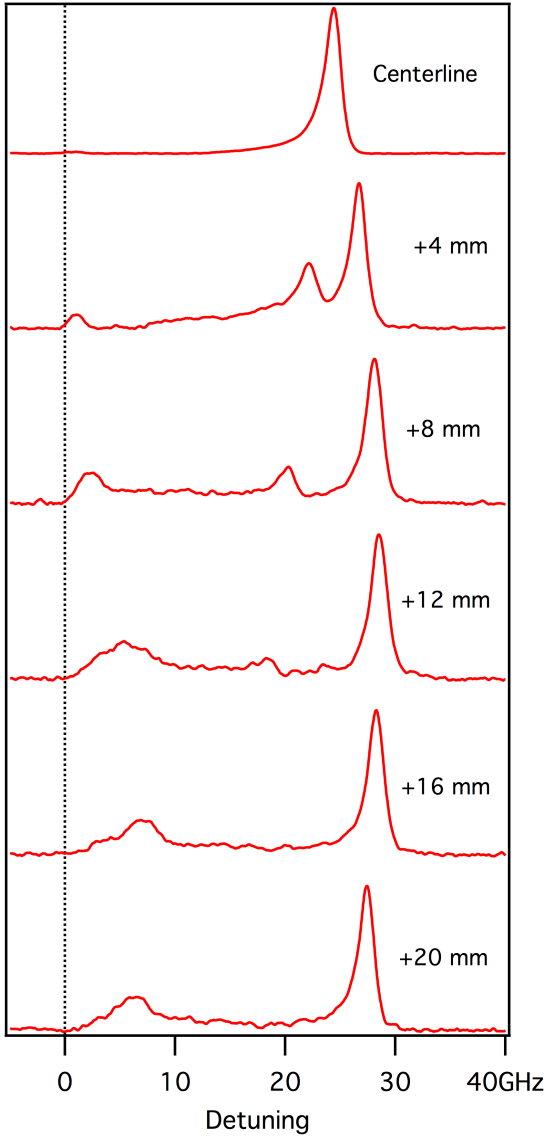


FIG. 11. Evolution of Kr II fluorescence lineshape at $Z = +13$ mm with distance from centerline (Y location) labeled. Note that all fluorescence curves are peak normalized.

tion of low energy ions nearby. The slight negative velocities (ranging from -200 to -400 m/s) in this region may be due to the cathode plume orientation and the visible plume emanating from the cathode orifice that visually appears to curve toward the anode. The mechanism for higher velocities in this population outside of $Z = \pm 10$ mm is not currently understood.

C. Velocity Distributions and Ion Temperatures

The mathematical extraction of VDF data requires the deconvolution of the laser line width and ion transition line shape from the raw fluorescence. This is somewhat

problematic when we look at the data extracted from the accelerated plasma. Throughout the acceleration channel, it is clear that ionization and acceleration processes overlap and are not separable. In the plume where the acceleration is essentially complete, the raw fluorescence lineshape bears a history of the acceleration process and interactions with either background neutrals of the vacuum chamber or other portions of the plume. In short, it is difficult to extract a mathematically pure VDF, or for similar reasons a temperature based on line shape.

However as previously stated, the raw fluorescence provides a usable estimate VDF. This is a viable alternative for a number of reasons. First, the raw fluorescence is relatively broad. Deconvolving using noise tolerant techniques such as Tikhonov regularization²³ has shown us that the VDF is not particularly different than the raw fluorescence traces mapped to velocity space using Eqn. 1 as previously demonstrated in Fig. 8. Our calculations show that deconvolution of a 1-2 GHz Gaussian line width for the transition and a 500 kHz line width for the laser does not appreciably change raw fluorescence. We estimate that the raw fluorescence only varies from the fully deconvolved VDF by at most 15% and then only for the sharpest peaks. This upper limit was determined based on previous measurements which showed that the ion temperatures, as near as they can be defined, are low as measured in radial measurements.² In fact, the lineshape in the axial direction actually appears to be dominated by discharge plasma dynamics and these are reflected in the axial fluorescence lineshape.²²

Determining useful ion temperatures is similarly difficult, as all the issues that hinder deconvolution also make temperature determination difficult. Adding to the difficulty is the non-equilibrium and turbulent nature of the plasma acceleration. It is demonstrable from plume emission measurements that the ionic states in xenon Hall effect thrusters are not in equilibrium with one another²⁴. Therefore, each ion electronic state may have a unique temperature due to the low plasma density resulting in little collisional equilibration. Furthermore, the ionization and acceleration zones are believed to shift locations due to a periodic axial traveling ionization wave²⁵. These two fundamental aspects of Hall type plasma accelerators complicate the extraction of clean lineshapes from the LIF data.

The measurement at $Y = +12$ and $Z = -13$ mm appears to be least affected by acceleration and is not as subject to mixing of velocity populations due to its location deep within the acceleration channel before significant acceleration has occurred. At this location, an ion temperature of 1,900 K is extracted using the entire lineshape. At $Z = -12$ mm, the temperature rises dramatically to 4,600 K. Further downstream, the effect of overlapped acceleration and acceleration strongly suggested the lineshape temperature analysis use the highest velocity portion of the peak. For all subsequent cases, the lineshape shown in Fig. 8 was sampled between 90% on the low velocity side of the peak to the baseline on the

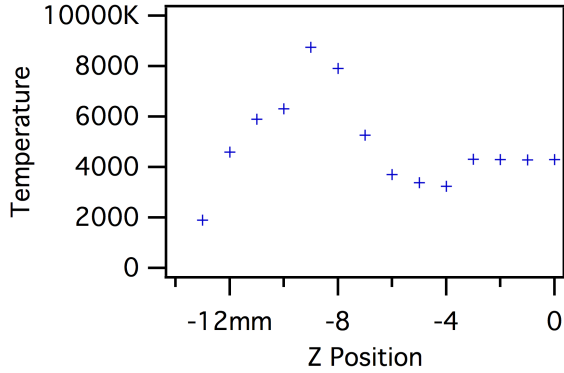


FIG. 12. Ion temperatures estimated from measured fluorescence within the acceleration channel ($Y = +12$ mm).

high velocity side of the peak. These measurements yield the results shown in Fig. 12.

The uncertainties of the ion temperatures in Fig. 12 are believed to be large for the reasons discussed previously and therefore should only be considered as providing general guidance as to the ion temperatures of the $5d^4D_{7/2}$ probed metastable state. To the extent that we can rely on the temperatures yielded by our analysis, the ion temperature is at its maximum at the same location where the ionization appeared most complete at $Z = -9$ mm. This is also very close to the measured peak electric field at $Z = -8$ mm. At the exit plane location of $Z = -7$ mm, the ion temperature has fallen to approximately 5,300 K. Just beyond the exit plane, the temperature further drops to 3,200 K. It then appears to rise and stabilize at 4,300 K further into the plume.

The trends in the ion temperature peaking where propellant ionization occurs due to energetic electron impact and dropping where primarily acceleration occurs are consistent with the processes within a Hall effect thruster. The ionic temperature rise just outside the thruster may be attributable to an over-expanded plume interacting with background neutrals; however, the inherent uncertainties of the measurement coupled to the small magnitude of the change make this somewhat speculative, even if consistent with the observations.

Due to the overlapping velocity populations in the plume, only the highest velocity feature was examined to determine temperature at the cathode plane ($Z = +13$ mm). Sampling the highest velocity population in the same way as within the acceleration channel, ionic temperatures were extracted with the intent of minimizing uncertainties due to the overlapping populations previously discussed. The results of these measurements, 20 mm downstream of the exit plane, are shown in Fig. 13. A sample error bar (± 200 m/s) demonstrates the uncertainty associated with the determination of the measurement baseline. The total uncertainty is substantially higher as previously discussed.

The ion temperatures at the cathode plane demon-

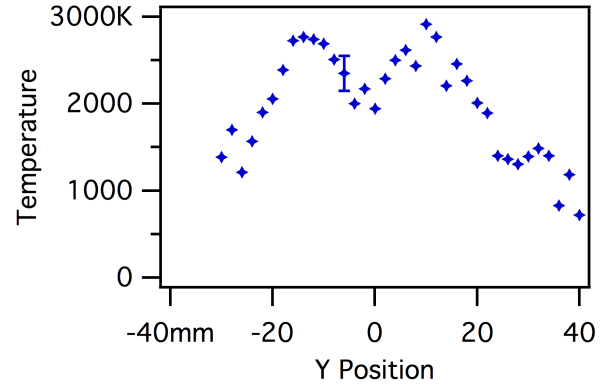


FIG. 13. Ion temperatures estimated from measured fluorescence of the highest velocity peak at the cathode plane ($Z = +13$ mm).

strate aspects consistent with temperatures just outside the thruster in Fig. 12 where temperatures of 4,200 K are measured 7 mm downstream of the exit plane ($Z = 0$ mm). Acceleration channel centerline temperatures peak at approximately 3,000 K in Fig. 13. The twin peaked distribution, indicative of the annular plasma discharge, is also consistent with expectations. Again, caution must be taken in the interpretation of these data. Although these values are consistent with the 0.45 eV (5,200 K) lower bound from emission measurements for a larger xenon Hall effect thruster at the exit plane²⁴, these measurements of the $5d^4D_{7/2}$ metastable state temperature should be viewed as only indicative of trends and not to be a true temperature of the entire ion populations in general.

VI. CONCLUSIONS

We have presented the Kr II $5d^4D_{7/2}-5p^4P_{5/2}^o$ transition at 728.98 nm as suitable for measuring the flow fields of a highly ionized krypton accelerated plasma using LIF. Our measurement survey of the near-plume and acceleration channel ion velocities of a cross-field acceleration type discharge, referred to as a *Hall effect thruster* in the spacecraft community, demonstrates that this optical transition is suitable for diagnosis of accelerated rarified krypton plasma streams. Use of this transition takes advantage of the highly populated $5d^4D_{7/2}$ metastable state to maximize signal strength while allowing use of commercially available external cavity diode lasers. Use LIF on the Kr II $5d^4D_{7/2}-5p^4P_{5/2}^o$ transition at 728.98 nm allowed for the identification of regions of ionization, quantification of the acceleration profile and effective electric field, and more cautiously an indication of the ion temperature of the Kr II $5d^4D_{7/2}$ state within a complex plasma discharge. It is these kinds of measurements that allow the non-intrusive characterization of low tempera-

ture accelerated plasmas such as the Hall effect thruster utilized on spacecraft propulsion where optimization for efficiency of energy conversion to momentum transfer and longevity are paramount.

VII. ACKNOWLEDGMENTS

The authors are thankful for a number of fruitful discussions that enabled this paper. This includes several early discussions with Dr. M. Cappelli of Stanford University and Dr. D. Scharfe at the Air Force Research Laboratory. Finally, the paper would not have been written except for the strong encouragement received very early from Dr. C. W. Larson who would have found this paper to be *classically OCD*!

- ¹D. R. Lide, *Handbook of Chemistry and Physics*, 79th ed. (CRC Press, 1998).
- ²W. A. Hargus Jr. and M. A. Cappelli, "Laser-induced fluorescence measurements of velocity within a hall discharge," *Applied Physics B* **72**, 961–969 (2001).
- ³W. A. Hargus and M. R. Nakles, "Ion velocity measurements within the acceleration channel of low-power hall thruster," *IEEE Transactions on Plasma Science* **36**, 1989–1997 (2008).
- ⁴W. Demtroder, *Laser Spectroscopy: Basic Concepts and Instrumentation* (Springer-Verlag, 1996).
- ⁵M. R. Nakles and W. A. Hargus Jr., "Background pressure effects on internal and near-field ion velocity distribution of the bht-600 hall thruster," in *Proceedings of the 44th Joint Propulsion Conference and Exhibit*, AIAA-2008-5101 (American Institute of Aeronautics and Astronautics, Hartford, CT, 2008).
- ⁶W. A. Hargus Jr., M. R. Nakles, B. Pote, and R. Tedrake, "The effect of thruster oscillations on axial velocity distributions," in *Proceedings of the 44th Joint Propulsion Conference and Exhibit*, AIAA-2008-4724 (American Institute of Aeronautics and Astronautics, Hartford, CT, 2008).
- ⁷T. Fujimoto and A. Iwamae, eds., *Plasma Polarization Spectroscopy*, Series on Atomic, Optical and Plasma Physics, Vol. 44 (Springer-Verlag, 2008).
- ⁸R. D. Cowan, *The Theory of Atomic Structure and Spectra* (University of California Press, Berkeley, CA, 1981).
- ⁹T. Trickl, M. J. J. Vrakking, R. Cromwell, Y. T. Lee, and A. H. Kung, "Ultrahigh-resolution (1+1) photoionization spectroscopy of kr i: Hyperfine structures, isotope shifts, and lifetimes for the $n = 5, 6, 7$ 4p5 ns rydberg levels," *Physica Review A* **39**, 2948–2955 (1989).
- ¹⁰I. I. Sobelman, *Atomic Spectra and Radiative Transitions* (Springer-Verlag, Berlin, 1992).
- ¹¹H. E. White, *Introduction to Atomic Spectra* (McGraw-Hill, New York, 1934).
- ¹²R. Cedolin, *Laser-Induced Fluorescence Diagnostics of Xenon Plasmas*, Ph.D. thesis, Stanford University (1997).
- ¹³D. B. Scharfe, *Alternative Hall Thruster Propellants Krypton and Bismuth: Simulated Performance and Characterization*, Ph.D. thesis, Stanford University, Palo Alto, CA (2009).
- ¹⁴T. J. Scholl, T. D. Gaily, R. A. Holt, and S. D. Rosner, "Fast-ion-beam laser and laser-rf double resonance measurements of hyperfine structure in 83kr ii," *Physica Review A* **33**, 2396–2400 (1986).
- ¹⁵H. A. Schuessler, A. Alousi, M. Idrees, Y. F. Li, F. Buchinger, R. M. Evans, and C. F. Fischer, "Isotope shifts and hyperfine-structure-splitting constants of the 4d-5p transition in kr ii at 729 nm," *Physica Review A* **45**, 6459–6467 (1992).
- ¹⁶Y. Ralachenko, A. E. Kramida, J. Reader, and N. A. Team, "Nist atomic spectra data base version 3.1.5," Tech. Rep. (National Institute of Standards and Technology, Gaithersburg, MD, 2010).
- ¹⁷I. Leybold-Heraeus Vacuum Products, *Vacuum Technology its Foundations Formulae and Tables* (Leybold-Heraeus Vacuum Products, Inc., 1987).
- ¹⁸W. A. Hargus and C. S. Charles, "Near exit plane velocity field of a 200 w hall thruster," *Journal of Propulsion and Power* **24**, 127–133 (2008).
- ¹⁹B. Barbieri, N. Beverini, and A. Sasso, "Optogalvanic spectroscopy," *Review of Modern Physics* **62**, 603–644 (1990).
- ²⁰M. R. Nakles, W. A. Hargus, J. J. Delgado, and R. L. Corey, "A performance comparison of xenon and krypton propellant on an spt-100 hall thruster," in *Proceedings of the 32nd International Electric Propulsion Conference*, 003 (Electric Rocket Society, Weisbaden, Germany, 2011).
- ²¹W. A. Hargus and C. S. Charles, "Near-plume laser-induced fluorescence velocity measurements of a medium power hall thruster," *Journal of Propulsion and Power* **26**, 135–141 (2010).
- ²²W. A. Hargus Jr. and M. R. Nakles, "Evolution of the ion velocity distribution in the near field of the bht-200-x3 hall thruster," in *Proceedings of the 42nd Joint Propulsion Conference and Exhibit*, AIAA-2006-4991 (American Institute of Aeronautics and Astronautics, Sacramento, CA, 2006).
- ²³W. H. Press, S. A. Teukolsky, W. T. Vetterling, and B. P. Flannery, *Numerical Recipes in Fortran 77: The Art of Scientific Computing*, 2nd ed. (Cambridge University Press, 1992).
- ²⁴D. H. Manzella, "Stationary plasma thruster plume emissions," in *Proceedings of the 23rd International Electric Propulsion Conference* (Electric Rocket Society, 1993).
- ²⁵E. Y. Choueriri, "Plasma oscillations in hall thrusters," *Physics of Plasmas* **8**, 1411–1426 (2001).